Supporting Information for "An evaluation of kilometer-scale ICON simulations of mixed-phase stratocumuli over the Southern Ocean during CAPRICORN"

Veeramanikandan Ramadoss[1], Kevin Pfannkuch[1], Alain Protat[2], Yi Huang[3,4], Steven Siems[5]and Anna Possner[1]

[1]Institute for Atmospheric and Environmental Sciences, Goethe University, Frankfurt, Germany

[2]Australian Bureau of Meteorology, Melbourne, Victoria, Australia

[3]The University of Melbourne, School of Geography, Earth and Atmospheric Sciences, Melbourne, VIC, Australia

[4]Australian Research Council Centre of Excellence of Climate Extremes, Melbourne, Australia

[5]Monash University, Melbourne, VIC, Australia

Contents of this file

Corresponding author: Veeramanikandan Ramadoss, Institute for Atmospheric and Environmental Sciences, Goethe University, Altenhöferallee 1, 60438, Frankfurt/Main, Germany. (ramadoss@iau.uni-frankfurt.de)

1. PAMTRA for ICON simulations

Passive and Active Microwave TRAnsfer (PAMTRA) is made to accommodate microphysical outputs from both 1M and 2M ICON simulations (Mech et al., 2020). The active radiative transfer part includes the forward simulation of the bottom-up radar reflectivity profiles, and Doppler spectrum and its moments. The 1M scheme that simulates prognostic mass mixing ratio is assumed to have a monodisperse particle size distribution for both cloud droplet and cloud ice hydrometeors. Inverse exponential size distribution is assumed for the other hydrometeor categories. The parameters of four-parameter gamma distribution are set to transform into a monodisperse (all the four parameters = 0) and inverse exponential size distribution (shape parameter = 0 and power factor = 1) (Petty & Huang, 2011; Wu & McFarquhar, 2018; Mech et al., 2020), with the maximum fixed size for the former and size computation according to mass-size power-law relation for the latter. All six hydrometeor categories in 2M are assumed to be distributed according to modified four-parameter gamma distribution, while the sizes are computed from mass using power-law relations. In our PAMTRA offline simulations, cloud droplets, rain, graupel and hail follow mie scattering, whereas ice and snow follow self-similar Rayleigh–Gans scattering.

2. Parameterization for cloud droplet number concentration

In 2M scheme, the cloud droplet number concentration (CDNC) at the cloud base is parameterized using the regression equations with CDNC as a function of condensation nuclei (CN) concentration, width of their size distribution and cloud base velocity (Segal & Khain, 2006). The number of droplets to be added in the cloud is provided by the look-up tables for a prescribed

list of number concentrations and mean radii of the CN size distribution, with the interpolated cloud base velocity and the width of CN distribution, making it prognostic in the 2M scheme.

3. Parameterization for ice crystal number concentration

In 2M scheme, the total potential ice nucleating particles (INPs) are determined based on the McCluskey, Ovadnevaite, et al. (2018) for sea spray aerosols (Equation 1) and Demott et al. (2015) for mineral dusts (Equation 2). The immersion freezing occurs in the region where the supersaturation with respect to ice is greater than 100%, the temperature is lower than -5°C, and the cloud droplet mass mixing ratio is higher than 1E-20 $\mathrm{kg\,m^{-3}}$.

$$n_{\mathrm{SSA\_INPs}}(T) = exp[-0.545(T - 273.15) + 1.0125] * S_{\mathrm{SSA}} * 0.001 \quad (1)$$

$$n_{\mathrm{dust\_INPs}}(T) = exp[0.46(273.15 - T) - 11.6] * (n_{500\mathrm{nm}})^{1.25} \quad (2)$$

Here, $\mathrm{n_{SSA\_INPs}}$ is the potential INP number concentration from the sea spray aerosols ($\mathrm{L^{-1}}$);

$\mathrm{n_{dust\_INPs}}$ is the potential INP number concentration from the mineral dust ($\mathrm{L^{-1}}$);

T is the temperature (K);

$\mathrm{S_{SSA}}$ is the surface area concentration of the sea spray aerosols ($\mathrm{m^2\,m^{-3}}$). The mean of $\mathrm{S_{SSA}}$ for the two-day period (=22.1829E-6 $\mathrm{m^2\,m^{-3}}$) is derived from McCluskey, Hill, et al. (2018);

$\mathrm{n_{500nm}}$ is the number concentration of mineral dust particles greater than 500 nm in size ($\mathrm{cm^{-3}}$). This value is calculated by equating the the total INP ($\mathrm{n_{SSA\_INPs}}$ + $\mathrm{n_{dust\_INPs}}$) number concentration as 0.0046 $\mathrm{L^{-1}}$ at -20°C (McCluskey, Hill, et al., 2018) in March-April 2016.

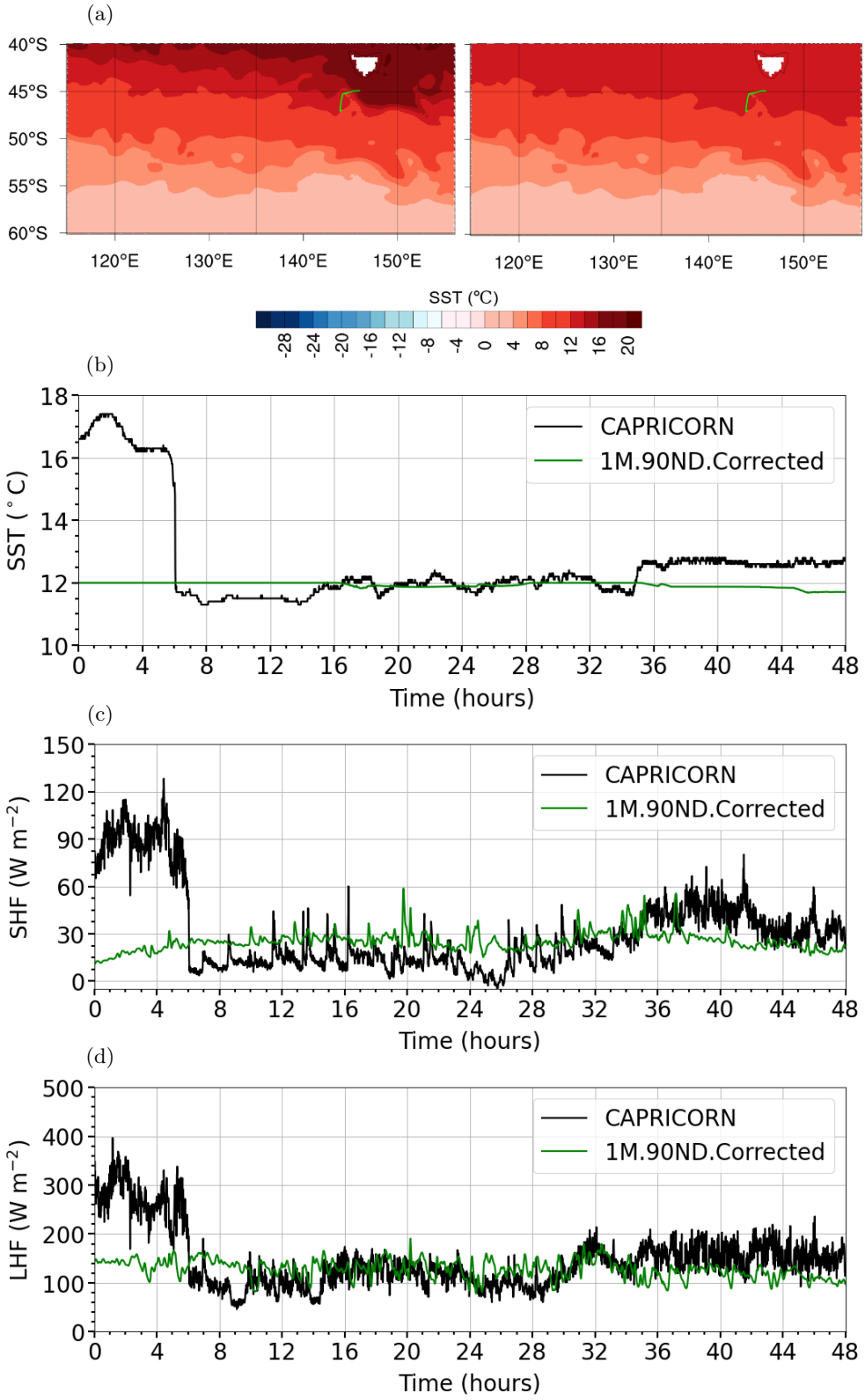

Figure S1: (a) Uncorrected (left-hand side) and corrected (right-hand side) SST contours in the simulation domain on 25th of March 2016 at 12:00:00 UTC with the two-day ship track (green). Time series for the entire ship track of (b) SST (°C), (c) SHF (W m^{-2}) and (d) LHF (W m^{-2}). SST, sea surface temperature; SHF, sensible heat flux; LHF, latent heat flux.

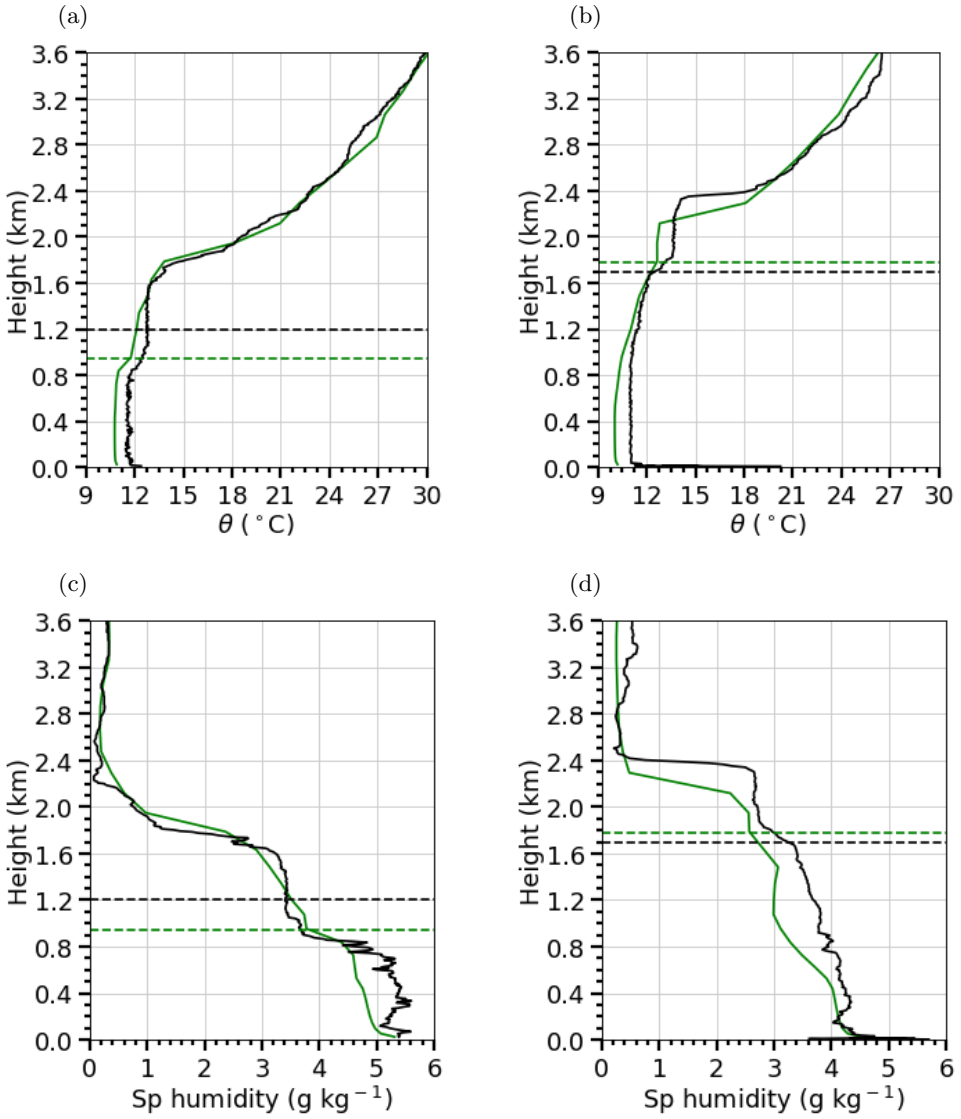

Figure S2: Thermodynamic profiles from upper-air radiosondes (black lines) and control simulation (1M.90ND - green lines) at the same location on (a),(c) 26th of March 2016 at 01:42:00 UTC and (b),(d) 26th of March 2016 at 06:24:00 UTC. Dashed lines in green (black) represent the location of simulated (observed) transition layer. θ represents potential temperature.

The boundary layer decoupling from the thermodynamic profile is identified by the presence of a transition layer that separates the cloud and subcloud layer. A strong decrease in mixing ratio and an increase in potential temperature characterize the transition layer. The conditional μ parameter which is defined as $\mu = \delta\ \theta\ /\ \delta$ P - ((0.608 θ /(1+0.608r)) δ r/ δ P) can identify the

presence of transition layer when the maximum value of 'μ' is positive below the main inversion and the ratio of the maximum value of 'μ' and its average below the main inversion is greater than 1.3 (Yin & Albrecht, 2000). Note that 'θ' is the potential temperature, 'r' is the mixing ratio, and 'P' is the atmospheric pressure.

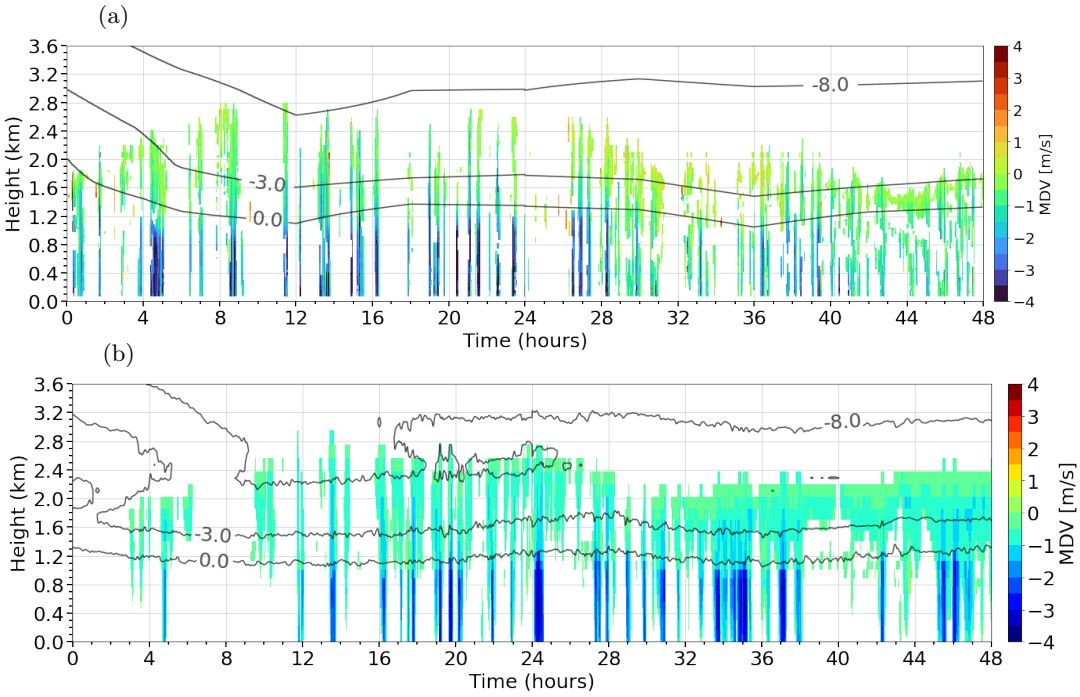

Figure S3: Time-height cross-section with 1 min temporal resolution of Mean Doppler Velocity for (a) CAPRICORN and (b) control simulation. Data is analyzed for the entire case study period (26th of March 2016 at 00:00:00 UTC to 28th of March 2016 at 00:00:00 UTC).

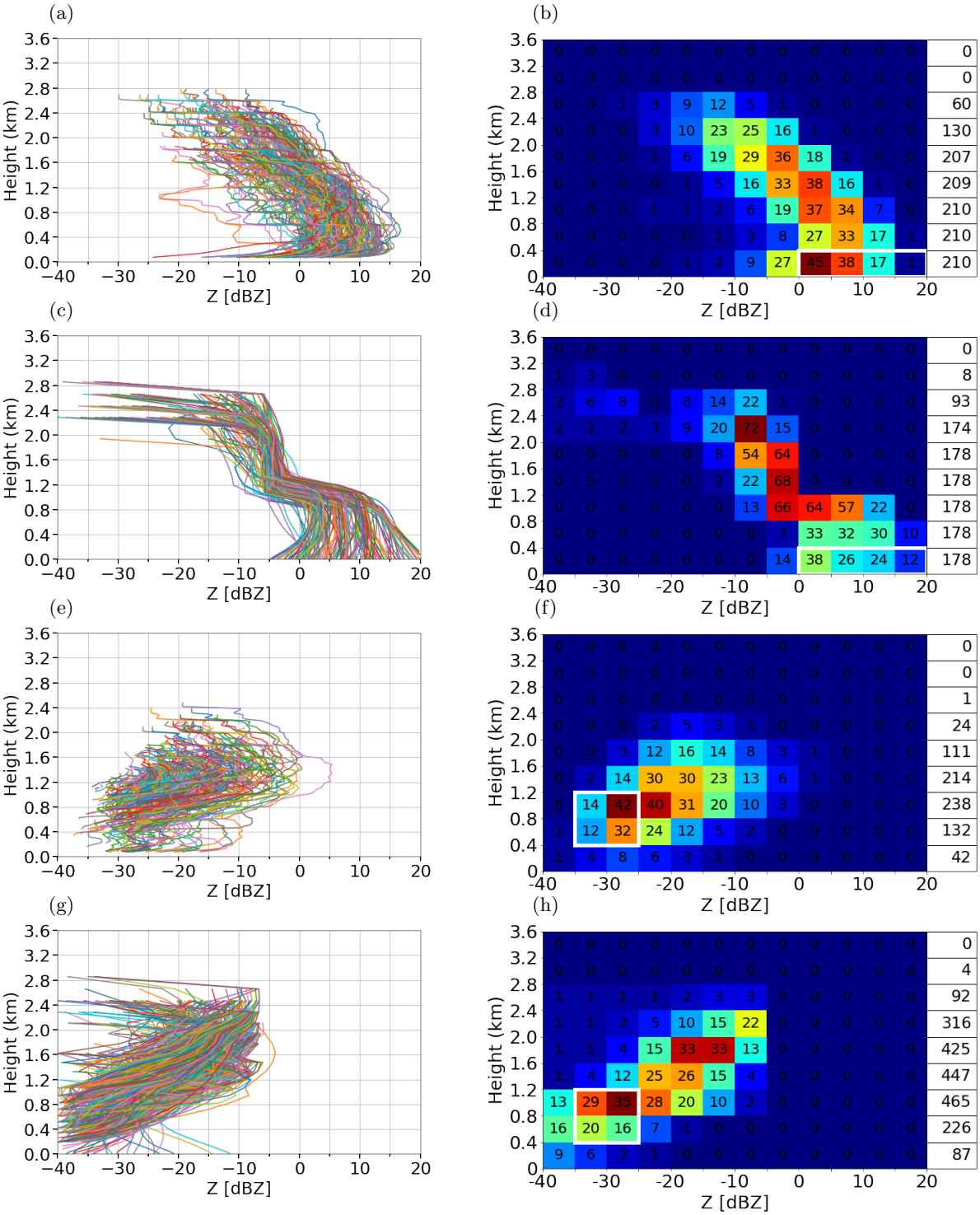

Figure S4: Along the ship track, all the continuous reflectivity streaks which are passing through the reflectivity bins enclosed by the white rectangles in (b),(d),(f),(h) are plotted with distinct coloured lines for (a),(e) CAPRICORN and (c),(g) control simulation. The number of streaks passing through each reflectivity-height bin is normalized with the total number of streaks passing through the white box (given in percentage - that shows how the streaks are distributed across the various bins) for (b),(f) CAPRICORN and (d),(h) 1M.90ND, with the total number of data for each height bin is shown on right. The reflectivity inside a certain height bin abruptly changes when the data across the reflectivity bins in that height bin exceeds 100%. Data is analyzed for the entire case study period (26^{th} of March 2016 at 00:00:00 UTC to 28^{th} of March 2016 at 00:00:00 UTC).

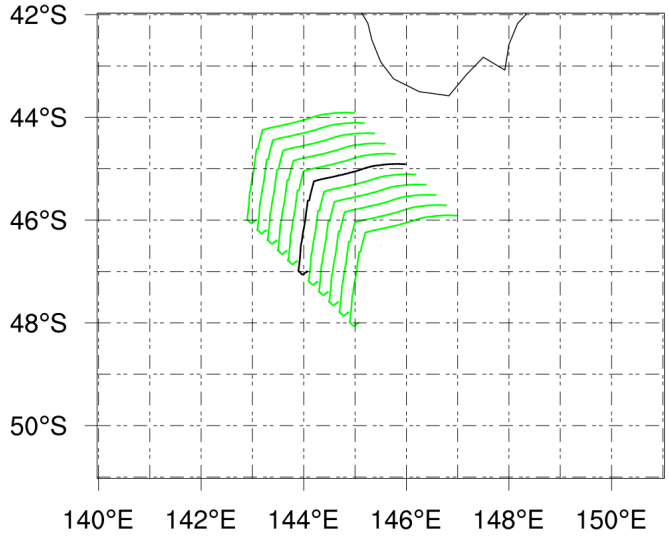

Figure S5: The two-day track (black) from CAPRICORN is offset (0.2°E, 0.2°S; 0.2°W, 0.2°N for each track) to 10 different locations (green) for quasi-ensemble analysis.

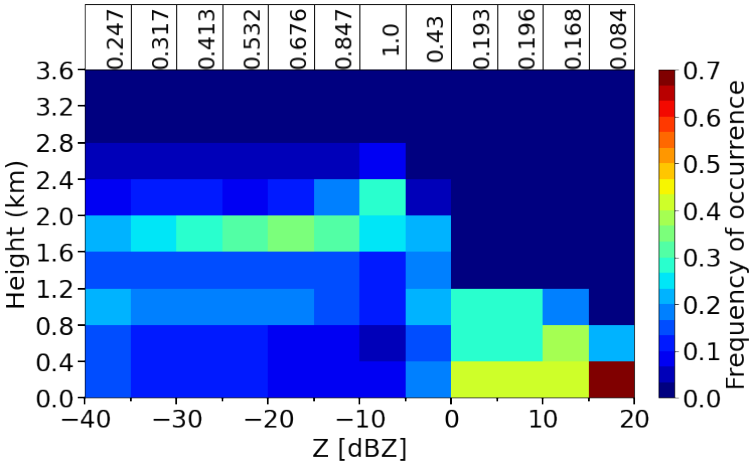

Figure S6: Normalized contoured frequency by altitude diagram with 1-min resolution for the quasi-ensemble control simulation.

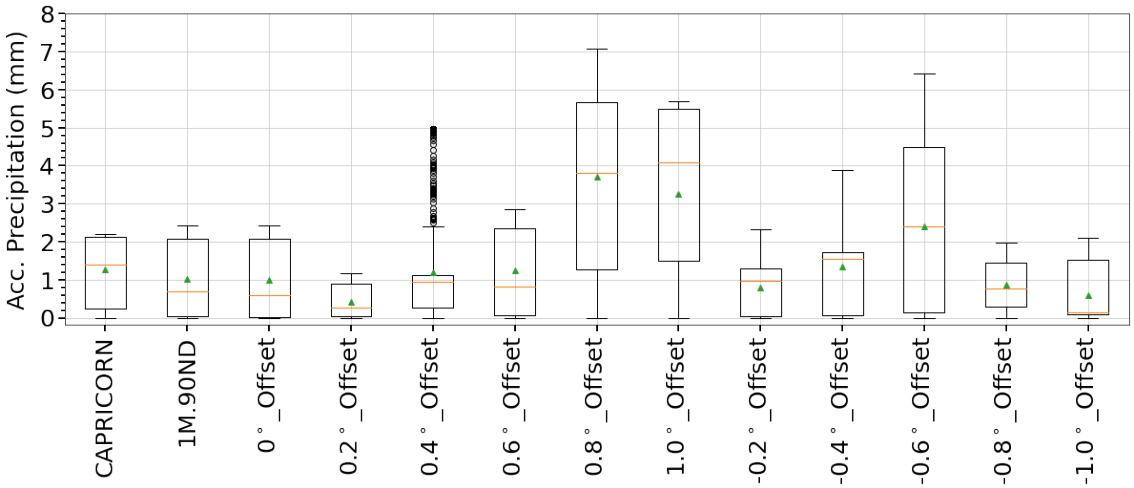

Figure S7: The spread of accumulated precipitation data for CAPRICORN, control simulation with data averaged for 2 km radius (1M.90ND) along the ship track and point data along the ship track at 10 different locations. The data from the track with no offset corresponds to 0°_Offset. The accumulated precipitation is analyzed in the tracks shifted to the south-east (0.2°_Offset, 0.4°_Offset, 0.6°_Offset, 0.8°_Offset and 1.0°_Offset) and the north-west (-0.2°_Offset, -0.4°_Offset, -0.6°_Offset, -0.8°_Offset and -1.0°_Offset) directions. Data is analyzed for the entire case study period (26th of March 2016 at 00:00:00 UTC to 28th of March 2016 at 00:00:00 UTC).

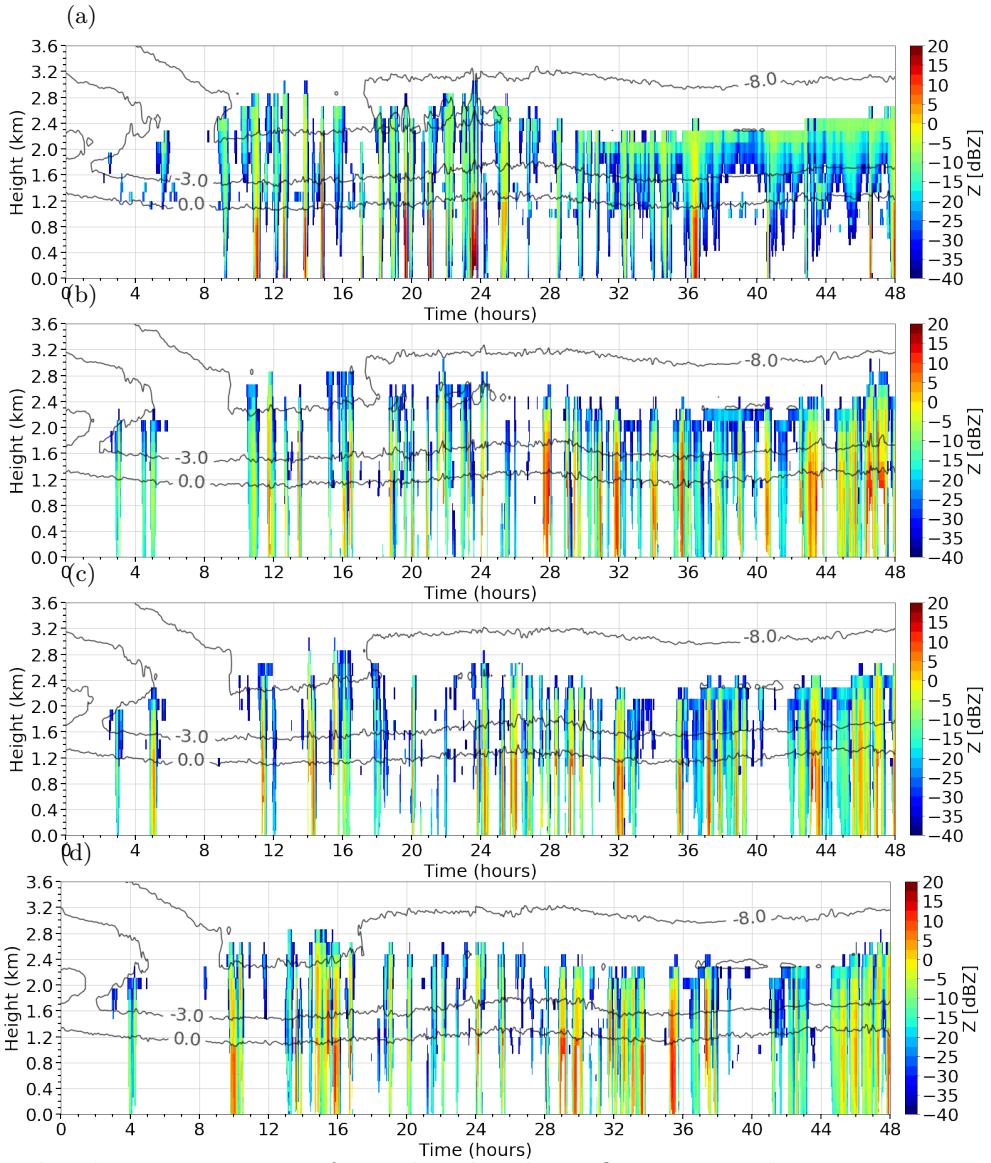

Figure S8: Time-height cross-section of simulated radar reflectivity with 1 min temporal resolution for (a) 1M.20ND, (b) 2M.P (c) 2M.HM and (d) 2M.HM.BR03. Case study period: 26th of March 2016 at 00:00:00 UTC to 28th of March 2016 at 00:00:00 UTC.

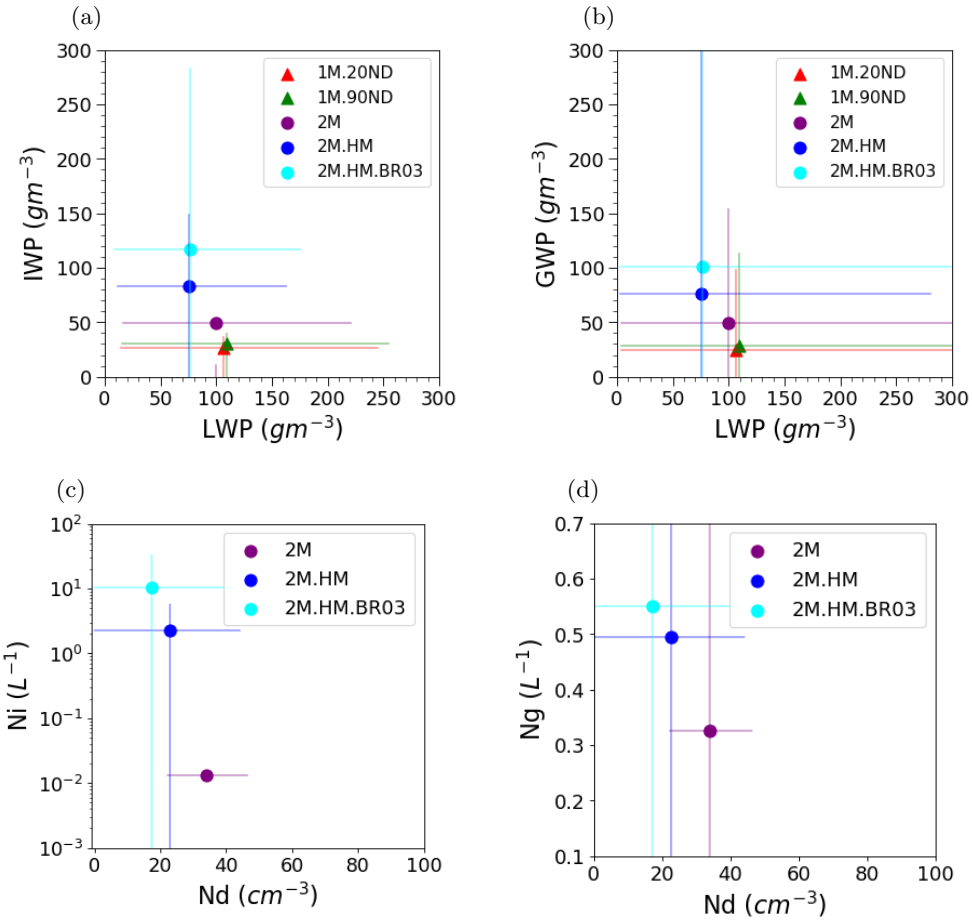

Figure S9: Spatial and temporal mean response obtained for the domain and case period of simulation in (a) IWP (all solid hydrometeors), (b) GWP, (c) ice number concentration (all solid hydrometeors), and (d) graupel number concentration. Domain is clipped around the ship track (see section 2.3).

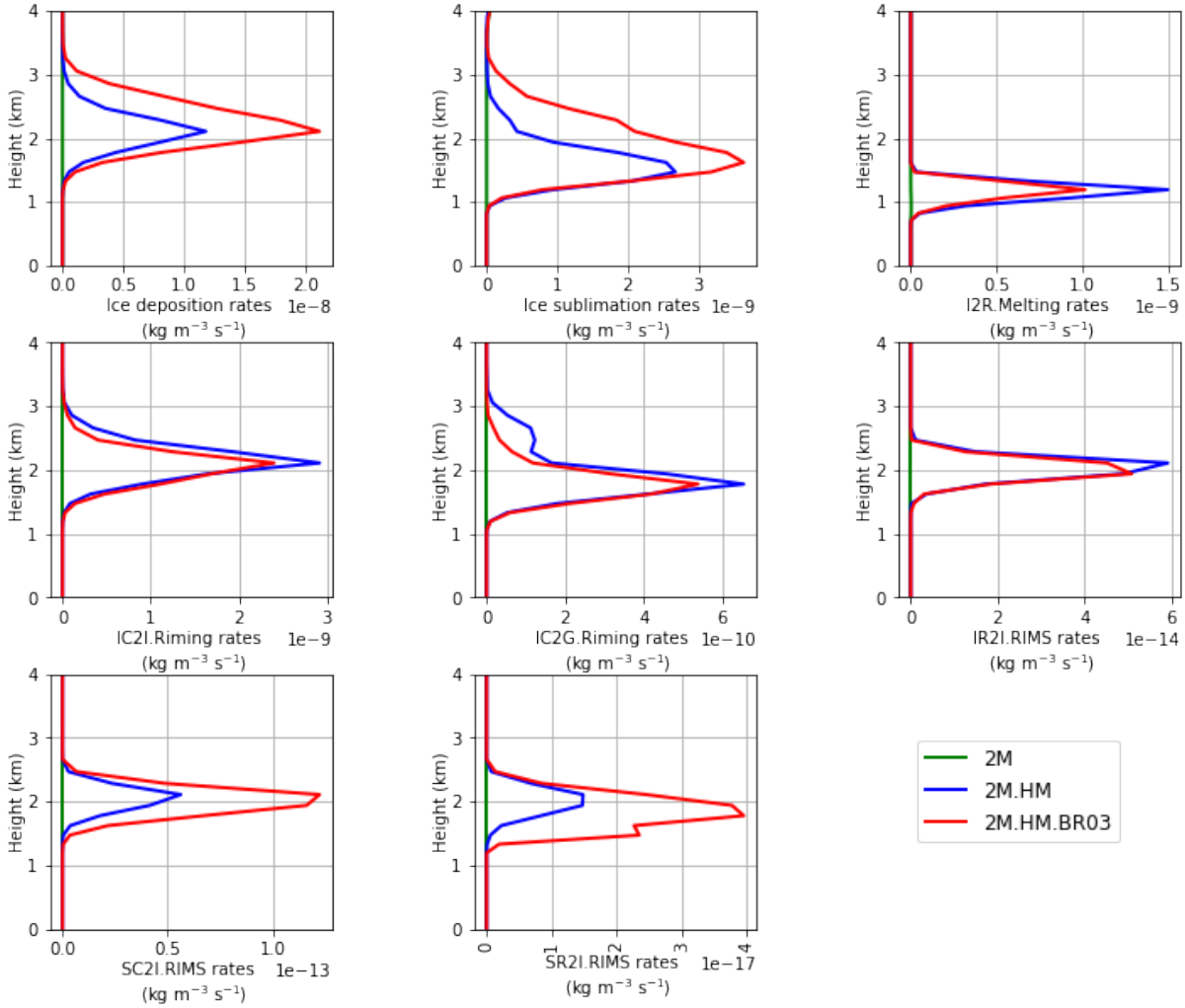

Figure S10: Spatial and temporal mean of ice microphysical processes for the entire simulation period (26th of March 2016 at 00:00:00 UTC to 28th of March 2016 at 00:00:00 UTC).

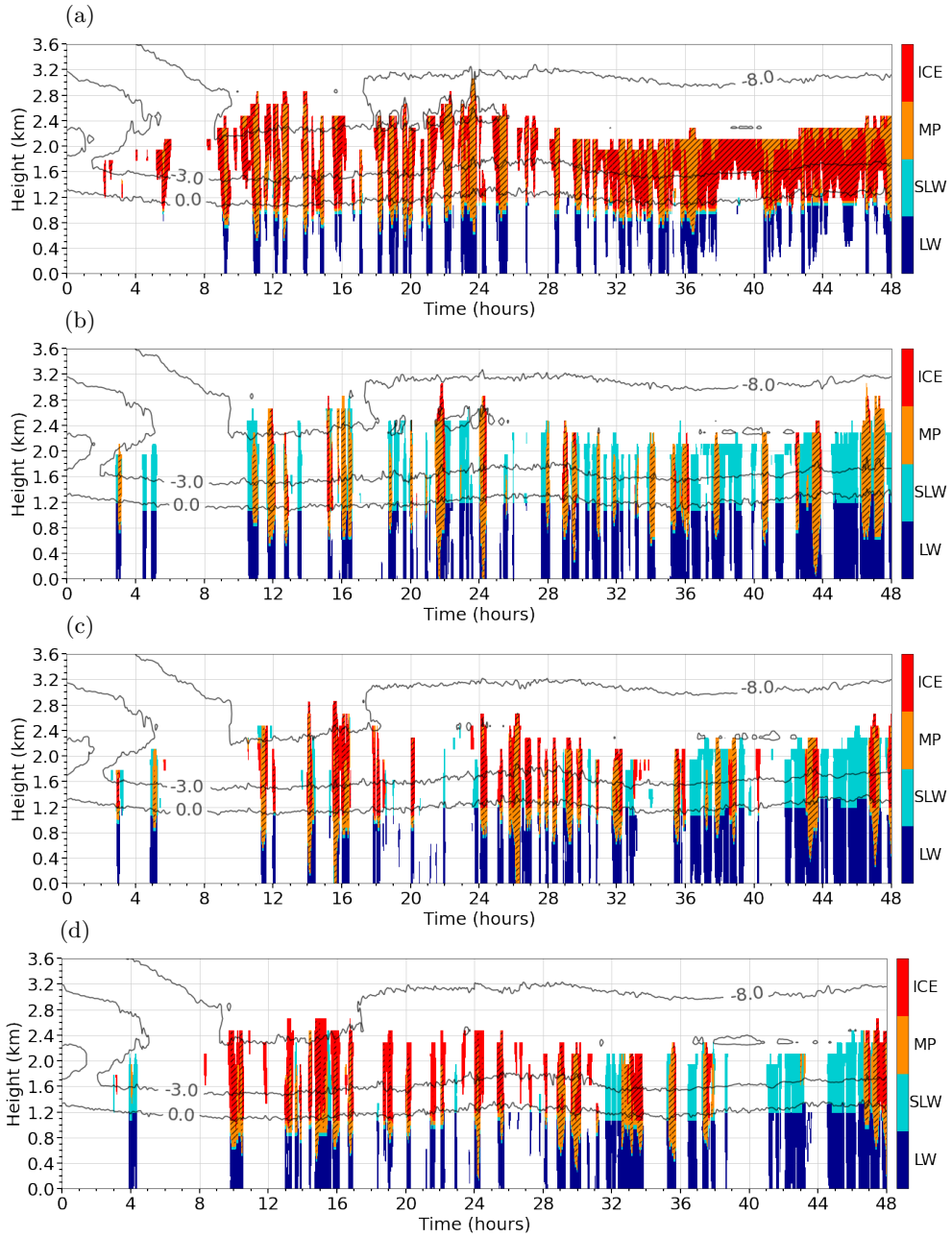

Figure S11: Time-height cross-section of simulated cloud-precipitation phase with 1 min temporal resolution for (a) 1M.20ND, (b) 2M.P (c) 2M.HM and (d) 2M.HM.BR03. Case study period: 26th of March 2016 at 00:00:00 UTC to 28th of March 2016 at 00:00:00 UTC.

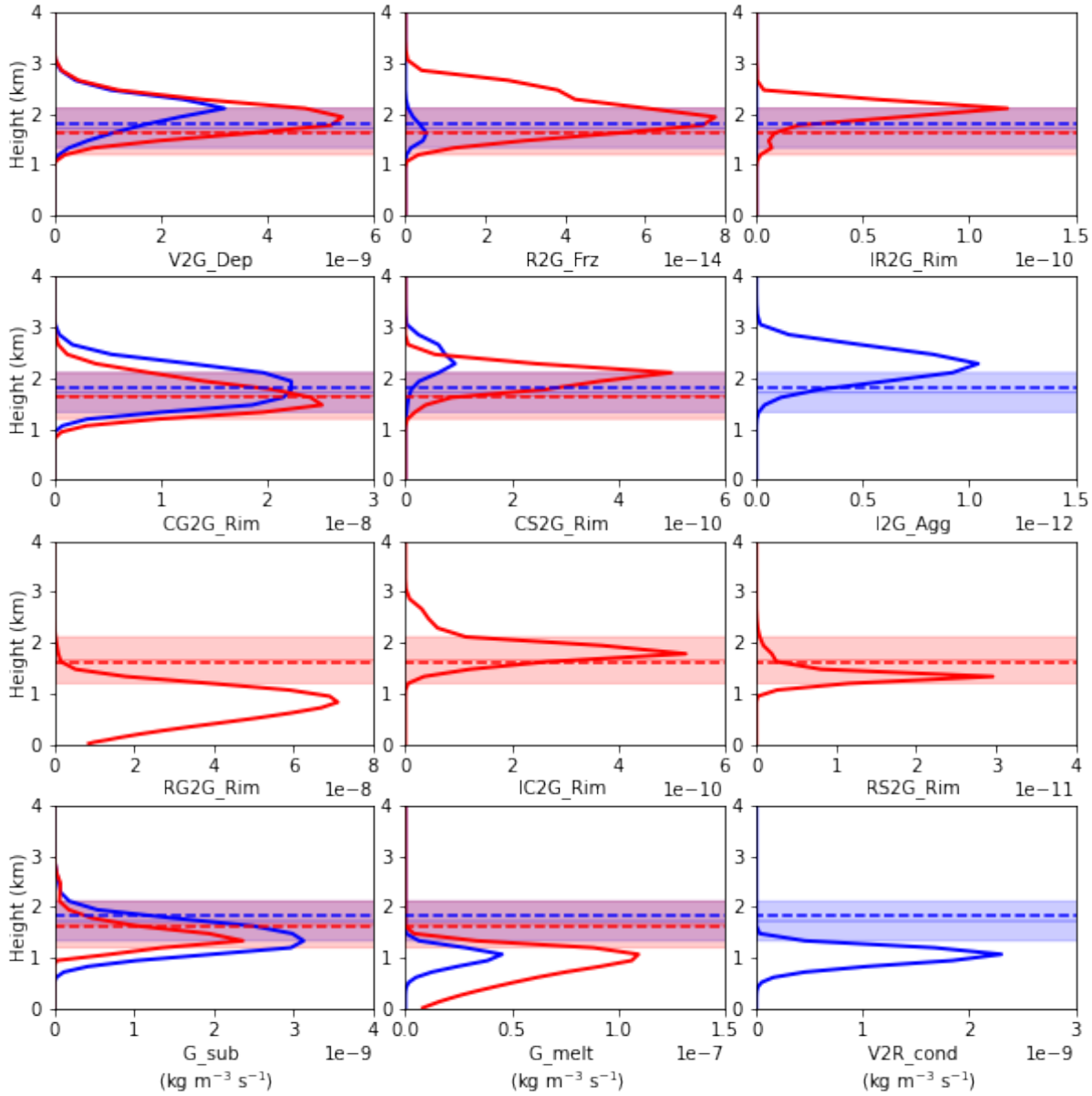

Figure S12: Spatial and temporal mean of graupel microphysical processes rates (solid lines). Dashed lines correspond to mean cloud base height. Blue and red lines represents 1M.90ND and 2M.HM simulation respectively. Shading corresponds to 20 to 80 percentile of CBH. The hourly data is processed only on 27th of March 2016.

(a)

Hydrometeor	1M.20ND (dBZ)	1M.90ND (dBZ)	2M.P (dBZ)	2M.HM (dBZ)	2M.HM.BR03 (dBZ)
All (normalized)	3.37	4.01	2.19	2.28	2.13
All	3689	3884	2174	2008	2060
Cloud water	1604	1822	579	254	367
Cloud ice	0	0	0	1296	1230
Rain	743	31	1940	921	973
Snow	3	16	0	942	1109
Graupel	3478	3665	612	756	750
Hail	-	-	10	0	0

(b)

Hydrometeor	1M.20ND (%)	1M.90ND (%)	2M.P (%)	2M.HM (%)	2M.HM.BR03 (%)
Cloud water	27.52	32.92	18.43	6.09	8.29
Cloud ice	0	0	0	31.09	27.77
Rain	12.74	0.56	61.76	22.09	21.96
Snow	0.05	0.29	0	22.59	25.03
Graupel	59.68	66.23	19.48	18.13	16.93
Hail	-	-	0.32	0	0

(c)

Hydrometeor	1M.20ND (%)	1M.90ND (%)	2M.P (%)	2M.HM (%)	2M.HM.BR03 (%)
All	-5.02	-	-44.03	-48.30	-46.96
Cloud water	-11.96	-	-68.22	-86.06	-79.86
Rain	2296.77	-	6158.06	2870.97	3038.71
Snow	-81.25	-	-100	5787.50	6831.25
Graupel	-5.10	-	-83.30	-79.37	-79.54

Table S1: Simulated bridge reflectivity analysis for the CFAD structure (-25 to 0 dBZ; 1.6 to 2 km altitude). (a) Sum of the reflectivities, (b) Percentage contribution of reflectivity of each hydrometeor with respect to the sum of individual reflectivities in every experiment and (c) Change in percentage compared to the control simulation (1M.90ND).

Experiment	Median (mm)	25^{th} percentile (mm)	75^{th} percentile (mm)
CAPRICORN	1.39	0.24	2.12
2km	0.68	0.03	2.07
0deg	0.59	0.01	2.06
0.2	0.26	0.04	0.89
0.4	0.95	0.25	1.11
0.6	0.82	0.07	2.35
0.8	3.81	1.28	5.66
1	4.10	1.50	5.50
-0.2	0.98	0.05	1.28
-0.4	1.54	0.06	1.72
-0.6	2.41	0.15	4.50
-0.8	0.76	0.29	1.44
-1	0.14	0.08	1.53

Table S2: The median, 25^{th} percentile and 75^{th} percentile of accumulated precipitation for CAPRICORN in the first row and the control simulation in all other rows. A mean value of precipitation within a 2 km radius is calculated in 1M.90ND for each coordinate along the ship track (Experiment '2km'). The point-wise precipitation data are retrieved for all other tracks (Experiment '0deg' to '-1'), with the number reflecting the degree of offset and the south-east offset being regarded a positive direction and the north-west offset being considered a negative direction.

Hydrometeor	Below_freezing_line		Above_freezing_line	
	min	max	min	max
All	-40	20	-40	0.2
Cloud water	-40	-6.6	-40	-6
Ice	-	-	-40	-25.4
Rain	-40	20	-40	-1.6
Snow	-	-	-40	-13.7
Graupel	-40	4	-40	3.8

Table S3: The reflectivity range (dBZ) for each hydrometeors for control simulation. The row 'All' represents when all the hydrometeors are active in reflectivity calculation. The tentative freezing line has been set at 1.2 km.

References

Demott, P. J., Prenni, A. J., McMeeking, G. R., Sullivan, R. C., Petters, M. D., Tobo, Y., ... Kreidenweis, S. M. (2015). Integrating laboratory and field data to quantify the immersion freezing ice nucleation activity of mineral dust particles. *Atmospheric Chemistry and Physics*, *15*(1), 393–409. doi: 10.5194/acp-15-393-2015

McCluskey, C. S., Hill, T. C., Humphries, R. S., Rauker, A. M., Moreau, S., Strutton, P. G., ... DeMott, P. J. (2018). Observations of Ice Nucleating Particles Over Southern Ocean Waters. *Geophysical Research Letters*, *45*(21), 11,989–11,997. doi: 10.1029/2018GL079981

McCluskey, C. S., Ovadnevaite, J., Rinaldi, M., Atkinson, J., Belosi, F., Ceburnis, D., ... DeMott, P. J. (2018). Marine and Terrestrial Organic Ice-Nucleating Particles in Pristine Marine to Continentally Influenced Northeast Atlantic Air Masses. *Journal of Geophysical Research: Atmospheres*, *123*(11), 6196–6212. doi: 10.1029/2017JD028033

Mech, M., Maahn, M., Kneifel, S., Ori, D., Orlandi, E., Kollias, P., ... Crewell, S. (2020). PAMTRA 1.0: The Passive and Active Microwave radiative TRAnsfer tool for simulating radiometer and radar measurements of the cloudy atmosphere. *Geoscientific Model Development*, *13*(9), 4229–4251. doi: 10.5194/gmd-13-4229-2020

Petty, G. W., & Huang, W. (2011). The modified gamma size distribution applied to inhomogeneous and nonspherical particles: Key relationships and conversions. *Journal of the Atmospheric Sciences*, *68*(7), 1460–1473. doi: 10.1175/2011JAS3645.1

Segal, Y., & Khain, A. (2006). Dependence of droplet concentration on aerosol conditions in different cloud types: Application to droplet concentration parameterization of aerosol conditions. *Journal of Geophysical Research Atmospheres*, *111*(15). doi: 10.1029/2005JD006561

Wu, W., & McFarquhar, G. M. (2018). Statistical theory on the functional form of cloud

particle size distributions. *Journal of the Atmospheric Sciences*, *75*(8), 2801–2814. doi: 10.1175/JAS-D-17-0164.1

Yin, B., & Albrecht, B. A. (2000, may). Spatial Variability of Atmospheric Boundary Layer Structure over the Eastern Equatorial Pacific. *Journal of Climate*, *13*(9), 1574–1592. Retrieved from http://journals.ametsoc.org/doi/10.1175/1520-0442(2000)013{\%}3C1574:SVOABL{\%}3E2.0.CO;2 doi: 10.1175/1520-0442(2000)013⟨1574:SVOABL⟩2.0.CO;2